Case Studies in Thermal Engineering 63 (2024) 105258

Contents lists available at ScienceDirect

Case Studies in Thermal Engineering

journal homepage: www.elsevier.com/locate/csite

Artificial intelligence and numerical study of the heat transfer and entropy generation analysis of NEPCM-MWCNTs-Water Hybrid Nanofluids inside a quadrilateral enclosure

Mohamed Bouzidi [a,b], Fathi Alimi [c], Aeshah Alasmari [d], Mohammad S. Islam [e,**], Pouyan Talebizadehsardari [f], Jana Shafi [g], Mehdi Ghalambaz [h,*]

[a] Department of Physics, College of Science, University of Ha'il, P.O. Box 2440, Ha'il, Saudi Arabia
[b] Laboratoire de Recherche sur Les Hétéro-Epitaxies et Applications, Faculty of Science of Monastir, University of Monastir, Monastir, 5019, Tunisia
[c] Department of Chemistry, College of Science, University of Ha'il, P.O. Box 2440, Ha'il, 81441, Saudi Arabia
[d] Department of Physics, College of Science, University of Bisha, Bisha, 61922, Saudi Arabia
[e] School of Mechanical and Mechatronic Engineering, University of Technology Sydney (UTS), 15 Broadway, Ultimo, NSW, 2007, Australia
[f] Power Electronics, Machines and Control (PEMC) Research Group, University of Nottingham, Nottingham, UK
[g] Department of Computer Engineering and Information, College of Engineering in Wadi Alddawasir, Prince Sattam Bin Abdulaziz University, Wadi Alddawasir, 11991, Saudi Arabia
[h] Department of Mathematics, Saveetha School of Engineering, SIMATS, Chennai, India

ARTICLE INFO

Keywords:
Entropy
Dense Neural Networks
Hybrid nanofluid
Nano-encapsulated phase change material (NEPCM)
Multi-walled carbon nanotubes (MWCNTs)

ABSTRACT

In the present investigation, the primary objective is to assess the synergistic impact of a novel hybrid nanofluid composed of nano-enhanced phase change material, multi-walled carbon nanotubes, and water. The governing equations are transformed into dimensionless forms for a more generalized analysis. To solve the problem, the Galerkin finite element method is employed, offering a robust numerical approach. A dataset of 1000 records was created by numerically solving the model for various combinations of control parameters. Using the dataset, a neural network was trained to learn the relationship between control parameters and heat transfer rate. The evaluation outcomes are comprehensively illustrated through key parameters, including local and average Nusselt numbers, total entropy generation, contours, and streamlines in the range of 10^3<Rayleigh number<10^5, 0<nanotube concentration<0.025, 0<nano capsule concentration <0.025, and 0.1<non-dimensional fusion temperature <0.7. Remarkably, the results indicate a substantial improvement in the heat transfer rate of the suspension for a hybrid concentration of 5 %, showcasing an impressive 13 % enhancement in contrast to the water host fluid's performance. Notably, the observed rise in entropy generation is relatively moderate, only a 5 % increase.

* Corresponding author.
** Corresponding author.
E-mail addresses: elbouzidimed16@yahoo.com (M. Bouzidi), alimi.fathi@gmail.com (F. Alimi), aymalasmari@ub.edu.sa (A. Alasmari), MohammadSaidul.Islam@uts.edu.au (M.S. Islam), pouyan.talebizadehsardari2@nottingham.ac.uk (P. Talebizadehsardari), j.jana@psau.edu.sa (J. Shafi), ghalambaz.mehdi@gmail.com (M. Ghalambaz).

https://doi.org/10.1016/j.csite.2024.105258
Received 15 June 2024; Received in revised form 3 October 2024; Accepted 8 October 2024
Available online 11 October 2024

Nomenclature

Latin letters	
Cp	Heat capacity per unit of mass (J/kg K)
Cr	Ratio of specific heats
f	Dimensionless melting function as described in Eq. (21)
g	Acceleration due to gravity (m^2/s)
h	Coefficient of heat transfer by convection (W/m^2 K)
k	Coefficient of thermal conductivity (W/m K)
L	Enclosure size (m)
l	Dimensionless enclosure size
Nu	Nusselt number
p	Pressure (Pa)
P	Dimensionless pressure
Pr	Prandtl number
Ra	Rayleigh number
S	Entropy generation
Ste	Stefan number
T	Temperature (K)
u	x-Velocity (m/s)
U	Dimensionless X-velocity
v	y-velocity (m/s)
V	Dimensionless Y-velocity
x	Horizontal Cartesian coordinate (m)
X	Non-dimensional horizontal Cartesian coordinate
y	Vertical Cartesian coordinate (m)
Y	Non-dimensional vertical Cartesian coordinate (m)
Greek symbols	
α	Thermal diffusivity (m^2/s)
β	Coefficient of thermal expansion (1/K)
δ	Non-dimensional indicator of the fusion range
μ	Dynamic viscosity of the fluid
θ	Dimensionless representation of temperature
λ	Ratio of specific heat capacities of NEPCM nanoparticles to the base fluid
ρ	Density of the material (kg/m^3)
φ	Volume fraction occupied by the nanoparticles, including simple and NEPCM types
ψ	Stream function defining fluid flow
Subscript	
b	Bulk properties of the suspension
c	Cold wall
f	Fusion property
h	Hot wall
hnf	Hybrid nanofluid
host	Base fluid
L	Local
NEPCM	Nano- Encapsulated phase change materials particles.
SNP	Simple nanoparticles
tot	Total value of the entropy generation including thermal and frictional terms

1. Introduction

The paramount importance of nanofluids, hybrid nanofluids, and nano-encapsulated phase change materials lies in their ability to enhance heat transfer rates, revolutionizing industries significantly. Nanofluids, comprising engineered nanoparticles, exhibit exceptional thermal conductivity, finding applications in electronics for efficient heat dissipation as well as mechanical equipment such as different types of heat exchangers with more thermal efficiency. Hybrid nanofluids, combining diverse nanoparticles, broaden their utility across industries, optimizing thermal management. NEPCMs contribute to efficient energy storage systems, benefiting the construction and automotive sectors, where superior heat transfer rates are vital for improved performance and energy efficiency.

Nanofluids, engineered colloids composed of base fluids and nanoparticles, have garnered significant attention due to their superior thermal properties. Buongiorno [1] established that nanofluids demonstrate enhanced thermal conductivity compared to their base fluids. The heat transfer coefficient's upsurge, surpassing predictions from traditional correlations like Dittus-Boelter's, has been attributed to factors beyond thermal conductivity. The study identified Brownian diffusion and thermophoresis as critical slip mechanisms in nanofluids. Buongiorno [1] proposed an alternative explanation, suggesting that nanofluid properties vary within the boundary layer due to temperature gradients and thermophoresis, resulting in decreased viscosity and enhanced heat transfer. Hussain and Hussein [2] assessed how copper-water nanofluid influences heat transfer by natural convection within a variably heated enclosure. Simulations revealed a substantial increase in Nusselt number with the addition of nanofluid. The study scrutinized various parameters such as Rayleigh numbers, tilted angles, aspect ratios, and solid volume fractions, demonstrating that nanofluid addition not only enhances heat transfer but also influences the shape of convection vortices, particularly with varying skew angles. Bouhalleb et al. [3] investigated natural convection heat transfer in a slanted cavity that was saturated with a CuO-Water nanofluid. The study numerically solved transport equations using the finite volume element method, exploring the impression of aspect ratio and Rayleigh number. The findings suggested that the Rayleigh number influence on the Nusselt number diminishes in shallow enclosures.

Kleinstreuer and Feng [4] have extensively reviewed experimental and theoretical works on enhancing nanofluid thermal conductivity. The review highlighted the issues regarding the best nanoparticle-liquid pairing, reliable measurement techniques, and consistent experimental data. It called for benchmark experiments using identical nanofluids subjected to different measurement methods and emphasized the need to consider multiple mechanisms in nanofluid heat transfer models.

Mohebbi et al. [4] employed the lattice Boltzmann method to study nanofluid free-convection inside an enclosure with rough elements. The study explored the numbers and parameters such as roughness elements aspect ratio and different values of nanoparticle concentration. Results indicated that the influence of roughness elements was more pronounced at higher Rayleigh numbers. In a numerical investigation by Snoussi et al. [5], convection heat transfer enhancement within a U-shaped cavity saturated by nanofluids was explored. The study considered two nanoparticle types (Cu and Al_2O_3) with host water. Results showed that heat transfer is augmented with higher values of nanoparticle concentration, Rayleigh numbers, and cooled wall length extensions. Rozati et al. [6] explored the effects of varying attack angles on free convection in an elliptical enclosure filled with water-Ag nanofluid. Their research focused on determining the most effective attack angle to enhance heat transfer efficiency. Findings indicate that altering attack angles markedly impacts the temperature distribution, highlighting how the enclosure's geometry plays a crucial role in modulating the Nusselt number.

While usual nanofluids are straightforward and consist of a single type of nanoparticle, hybrid nanofluids offer enhanced versatility and tailored properties by combining different nanoparticles, making them suitable for a more comprehensive array of applications that require specific fluid characteristics. Several recent studies investigated the heat transfer of hybrid nanofluids in enclosures. For instance, initial investigations in a quadrantal enclosure saturated with a porous medium and experiencing internal heat generation revealed key insights [7]. It was shown that the average Nusselt number escalates with increasing Rayleigh numbers and nanoparticle concentrations. Moreover, a notable interaction between heat generation parameters and the Rayleigh number significantly influences heat transfer rates, which is essential for enhancing heat exchangers and solar collectors [7]. In parallel research, a study conducted in a trapezoidal area affected by a magnetic field found that hybrid nanofluids could reduce entropy generation significantly while efficiently managing energy transport across varying intensities and orientations of the magnetic field [8]. This research highlights the critical role of magnetic fields in modulating thermal properties and stabilizing the convective behavior of hybrid nanofluids.

Recent researches have examined the natural convection dynamics under complex geometrical and reactive scenarios. For example, using the Prabhakar fractional model, the effectiveness of kerosene oil-based hybrid nanofluids infused with ferric oxide and zinc oxide nanoparticles in boosting heat transfer was demonstrated, a critical aspect for their use in energy sectors and automotive cooling systems [9]. Another examination showcased the advantageous use of hybrid nanofluids in tackling pollution and breaking down substances, as seen with aluminum oxide and copper nanoparticles enhancing convective heat transfer and aiding in pollutant decomposition within porous environments [10]. Additionally, exploring the interaction of chemical reactions and magnetic influences in a wavy-walled, porous cavity, it was found that hybrid nanofluids could reach elevated temperatures and create more dynamic streamlines under specific conditions, thereby proving their efficiency in improving natural convection heat transfer in environments that are chemically reactive and subject to magnetic disturbances [11].

Han et al. [12] introduced a novel carbon sphere/nanotube (CNTs) hybrid particles of diverse CNTs bonded to an Al_2O_3/Fe_3O_4 sphere. This innovative nanoparticle design aims to mitigate thermal contact resistance between CNTs, a common limitation in nanofluid applications. The hybrid structure facilitates rapid heat transport between CNTs through the central sphere, enabling more efficient thermal conductivity than conventional CNTs suspended in a host fluid. The overall performance of nanofluids is hindered by the interfacial thermal resistance between CNTs and the fluid, even though CNTs exhibit remarkably high thermal conductivity. The

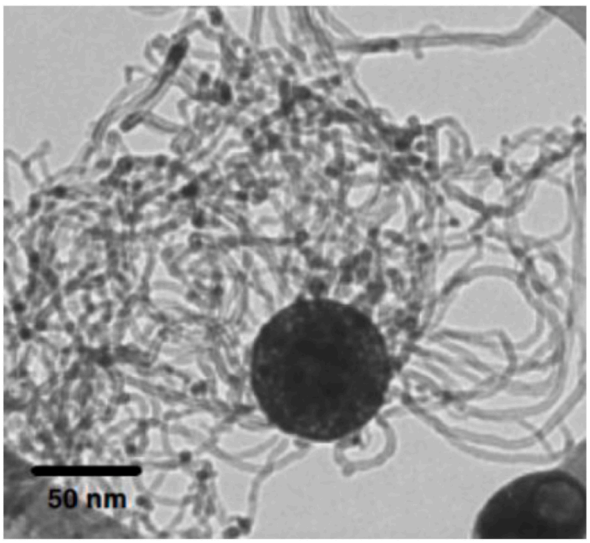

Fig. 1. A TEM view of sphere nanoparticles/CNTs provided by Han et al. [12].

composition shown in Fig. 1 is illustrated through a transmission electron microscopy image that depicts the thermal pathway of the hybrid nanoparticle, consisting of an AL_2O_3/Fe_3O_4 sphere combined with CNTs.

Reddy et al. [13–15] have evaluated the CNTs impressions on the heat and fluid flow in the different contributions. The effect of CNTs nanoparticles on the water based nanofluids around the vertical cone have been analyzed by Reddy [13]. Once, single walled nanotubes (SWCNTs) and once again, multi-walled ones (MWCNTs) were taken into the accounts. Moreover, the chemical reaction, radiation and MHD effects were under consideration. One of the most important results obtained in Reddy's study [13] shows that the heat transfer rate gets a higher growth through MWCNTs against SWCNTs. Reddy and Sreevedi [14], have considered a square cavity saturated by Ethylene- Glycol- MWCNTs nanofluid and modified Fourier heat flux. They [14] reveal that adding 3 % volume fraction of the MWCNTs nanoparticles within the host fluid amplifies heat transfer rate about 8 %. As a numerical study, heat and fluid flow irreversibility of MWCNTs- Water nanofluid in the square cavity in the presence of radiation and MHD impressions have been analysis [15]. To do it, the finite difference method was applied. The authors [15] found that appending 4 % volume fraction of the nanoparticles can make a heat transfer enhancement percentage more than 7 %.

Tayebi and Chamkha [16] conducted research on heat transfer via MHD free convection within a quadrilateral enclosure using an Al_2O_3-Cu/Water hybrid nanofluid. The study introduced a circular conductive cylinder that influenced the heat and fluid flow, underscoring the critical role of the corrugated conductive block in modifying the system's thermal behavior. Chabani et al. [17] performed a numerical analysis on the flow of MHD hybrid nanofluid in a modified trapezoidal porous cavity, using Ag and Al_2O_3 nanoparticles dispersed in water. Their findings highlighted that increasing Rayleigh and Darcy numbers could significantly boost the average Nusselt number and thermal transfer, potentially enhancing thermal efficiency. Rahman et al. [18] investigated the impact of thermal buoyancy on heat transfer in a rectotrapezoidal enclosure using an Al_2O_3-Cu/water hybrid nanofluid. They discovered that optimal thermal performance was achieved at lower Rayleigh numbers. Kadhim et al. [19] explored buoyancy-driven flow in a porous cavity with sinusoidal walls filled with a Cu-Al_2O_3/Water hybrid nanofluid under the local thermal non-equilibrium model. Key variables affecting the fluid flow and temperature distribution included the Darcy number, modified conductivity ratio, and nanoparticle volume fraction. Alsabery et al. [20] studied free convection in a wavy enclosure containing a heat source and Cu–Al_2O_3/-Water hybrid nanofluid. Their research established a direct correlation between the length of the heat source and the Nusselt number, with the hybrid nanofluid significantly outperforming pure water in heat transfer rates.

Hidki et al. [21] conducted a study on free convection within a quadrilateral enclosure filled with a Cu-Al_2O_3/H_2O hybrid nanofluid. The enclosure was heated using two solid blocks. Their findings indicated that increasing the Rayleigh number and incorporating hybrid nanoparticles led to a decrease in temperature, thus facilitating better heat exchange. Sreevedi and Reddy [22] in a numerical and dimensionless study, have evaluated radiative- MHD hybrid nanofluid inside a quadrilateral enclosure. SWCNTs and Al_2O_3 as nanoparticles and Ethylene Glycol as host fluid were selected. To solve the problem, finite difference scheme was considered. Reaching to a better heat transfer rate through SWCNTs nanoparticles versus Al_2O_3 ones is the pivotal result which is obtained in Sreevedi and Reddy's study [22]. On a related note, Scott et al. [23,24] carried out a series of experiments to explore the influence of Al_2O_3-MWCNT water-based hybrid nanofluids on heat transfer. They discovered that a nanoparticle volume concentration of 0.10 % could improve heat transfer efficiency by 49.27 %, underscoring the beneficial impact of hybrid nanofluids on the enhancement of natural convection processes [23].

Extensive research has been conducted on utilizing nano-encapsulated phase change materials (NEPCMs) in diverse heat transfer applications, demonstrating their potential to enhance thermal energy storage ability. Reddy et al. [25] have considered a thermal energy storage system and significantly improved heat transfer rate via dispersing a specified value of NEPCMs nanoparticles in the host fluid. Leading to a better heat transfer rate through the higher values of Stefan number was one the influent results obtained by the authors [25]. In another study by Reddy and Sreedevi [26], a quadrilateral thermal energy storage chamber was contained radiative MHD- NEPCMs nanofluid. The irreversibility was measured via entropy generation as well. They [26] determined that the melting process of the NEPCMs gets a more time by larger values of fusion temperature parameter (θ_f). Li et al. [27] proposed a novel shape-stabilized phase change material composite, a porous medium, utilizing copper (Cu) metal foam embedded with NEPCM. The composite exhibited a maximum wall temperature reduction of 47 °C compared to pure NEPCM, showcasing the synergistic effects of metal foam's thermal enhancement and NEPCM's latent heat absorption. In addition, with lower porosity, the composite displays improved performance. Mebarek-Oudina et al. [28] numerically investigates entropy generation and heat transfer in MgO-Al_2O_3/-water hybrid nanofluid within a porous elliptical cavity under a magnetic field. Results show enhanced heat transfer but increased irreversibilities. Alomari et al. [29] focused on the nuclear industry and proposed a wavy porous cavity saturated by MHD-NEPCM nanofluid. In addition, two hot cylinders have been demonstrated in the model. They [29] found that the heat transfer rate is an increasing and decreasing function of MHD effect and nanoparticles volume fraction, respectively.

Natural convection around a localized heated cylinder within a quadrilateral cavity containing NEPCM-water hybrid nanofluids was probed by Saleh et al. [30]. The hybrid nanofluid, consisting of NEPCM suspended in water, demonstrated an augmented Nusselt number over 10 % when 1 % of hybrid nanoparticles were suspended. The study highlighted the potential of such hybrid fluids for improving natural convection heat transfer. Turki et al. [31] simulated the NEPCM-water nanofluid thermal performance in a square cavity in the presence of a heat source relevant to electronic devices. The study revealed that the optimum heat transfer rate occurs at a dimensionless melting temperature of 0.3, independent of the Rayleigh number. Moreover, adding NEPCMs to the base fluid improved heat transfer by 12.5 %.

The topic of NEPCM suspensions is relatively new, with recent studies beginning to examine convection heat transfer in these suspensions within various enclosures. While the impact of the phase change of NEPCMs has been examined on heat transfer in several literature studies, the NEPCM suspensions were consist of one single type of nanoparticles (NEPCM particles). However, the mixture of a NEPCM and other types of nanoparticles can provide mix properties such as improved thermal conductivity and improved heat

capacity. Currently, the exploration of hybrid NEPCM suspensions, has remained largely uncharted. Incorporating MWCNTs is critical as it significantly boosts overall heat transfer efficiency. Additionally, NEPCM plays a crucial role in the absorption and release of latent heat, which affects convective heat transfer dynamics within the enclosure. Therefore, this study aims to conduct the first-ever analysis of natural convection heat transfer and entropy generation using MWCNTs-NEPCM hybrid nanofluids in a quadrilateral enclosure.

2. Model description and mathematical formulation

2.1. Model description

According to Fig. 2, the enclosure under consideration involves a host fluid flow, water, comprising two types of nanoparticles. The first type is devoid of phase change and is determined as MWCNTs, while the second type consists of NEPCM. Indeed, the NEPCM/MWCNTs combination obeys Han et al. [12] model (as seen in Fig. 2). Moreover, it is established that there is no chemical or physical interaction between the two types of nanoparticles, maintaining their distinct characteristics within the host fluid. The enclosure is distinguished by its vertical walls, with the left and right sides serving as the hot (T_h) and cold (T_c) boundaries, respectively. The horizontal walls are entirely insulated. Importantly, the enclosure's wall thickness is assumed to be neglected, and the no-slip condition is considered. The familiar Boussinesq approximation is employed to model the buoyancy force.

Table 1 contains the thermophysical properties of the applied materials in the quadrilateral enclosure. Notably, nonadecane and polyurethane comprise the core and shell of the NEPCM, respectively. The high value of the nonadecane specific heat-capacity, Cp, as a PCM is obvious. On the other hand, utilizing MWCNTs with exemplary thermal conductivity, k (w/m K), can also make a comprehensive suspension.

2.2. Mathematical formulation

By considering the assumptions discussed earlier and the model description, the governing equations are explained in their dimensional form as follows [37,38]:

Continuity

$$\frac{\partial u}{\partial x}+\frac{\partial v}{\partial y}=0 \tag{1}$$

Momentum components

$$\rho_{hnf}\left(u\frac{\partial u}{\partial x}+v\frac{\partial u}{\partial y}\right)=-\frac{\partial p}{\partial x}+\mu_{hnf}\left(\frac{\partial^2 u}{\partial x^2}+\frac{\partial^2 u}{\partial y^2}\right) \tag{2}$$

$$\rho_{hnf}\left(u\frac{\partial v}{\partial x}+v\frac{\partial v}{\partial y}\right)=-\frac{\partial p}{\partial y}+\mu_{hnf}\left(\frac{\partial^2 v}{\partial x^2}+\frac{\partial^2 v}{\partial y^2}\right)+g\rho_{hnf}\beta_{hnf}(T-T_c) \tag{3}$$

and energy (thermal) one

$$(\rho C_p)_{hnf}\left(u\frac{\partial T}{\partial x}+v\frac{\partial T}{\partial y}\right)=k_{hnf}\left(\frac{\partial^2 T}{\partial x^2}+\frac{\partial^2 T}{\partial y^2}\right) \tag{4}$$

where, ρ_{hnf}, μ_{hnf}, β_{hnf}, $C_{p,hnf}$, and k_{hnf}, are density, dynamic viscosity, thermal expansion volume coefficient, specific heat capacity, and thermal conductivity of the hybrid nanofluid, respectively. The related boundary conditions in a mathematical format have been determined in the set of equation (5):

$$x=0 \;\rightarrow\; T=T_h, u=v=0 \tag{5-a}$$

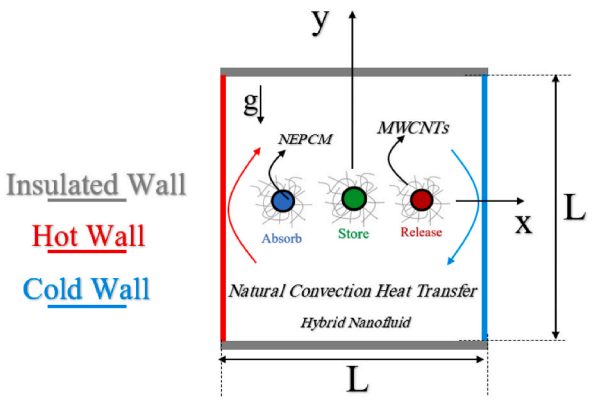

Fig. 2. A view of the physical model and the applied boundary conditions.

Table 1
Details the thermophysical attributes of the materials under consideration, as cited from Refs. [32–36].

Material	ρ (kg/m^3)	C_p (J/kg.K)	k (W/m.K)	β (K^{-1})	μ (kg/m.s)
Nonadecane (As core of NEPCM)	721	2037	–	–	–
Polyurethane (As shell of NEPCM)	786	1317.7	0.05	17.28×10^{-5}	–
Host fluid (water)	997.1	4179	0.613	21×10^{-5}	8.9×10^{-4}
MWCNTs	2100	711	3000	–	–

$$x = L \;\rightarrow\; T = T_c, u = v = 0 \tag{5-b}$$

$$\left.\frac{\partial T}{\partial y}\right|_{y=0} = 0, u = v = 0 \tag{5-c}$$

$$\left.\frac{\partial T}{\partial y}\right|_{y=L} = 0, u = v = 0 \tag{5-d}$$

In addition, total entropy generation, including thermal, and frictional localized terms, is extracted [33]:

$$s_l = s_{thermal} + s_{friction} = \frac{k_{hnf}}{T_0^2}\left[\left(\frac{\partial T}{\partial x}\right)^2 + \left(\frac{\partial T}{\partial y}\right)^2\right] + \frac{\mu_{hnf}}{T_0}\left(2\left(\left(\frac{\partial u}{\partial x}\right)^2 + \left(\frac{\partial v}{\partial y}\right)^2\right) + \left(\frac{\partial u}{\partial y} + \frac{\partial v}{\partial x}\right)^2\right) \tag{6}$$

In equation (6), the terms $S_{thermal}$ and $S_{friction}$ are utilized to determine the entropy generation arising from gradients in temperature and inter-layer fluid friction, respectively. To obtain The density, ρ_{hnf}, and heat capacity, $(\rho C_p)_{hnf}$ of the hybrid nanofluid, equations (7) and (8) are introduced [39]:

$$\rho_{hnf} = \varphi_{NEPCM}\rho_{NEPCM} + \varphi_{SNP}\rho_{SNP} + (1 - \varphi_{hnf})\rho_{host} \tag{7}$$

$$(\rho C_p)_{hnf} = \varphi_{NEPCM}(\rho C_p)_{NEPCM} + \varphi_{SNP}(\rho C_p)_{SNP} + (1 - \varphi_{hnf})(\rho C_p)_{host} \tag{8}$$

The thermal expansion volume coefficient of the hybrid nanofluid, β_{hnf}, can be evaluated as:

$$\beta_{hnf} = \varphi_{NEPCM}\beta_{NEPCM} + \varphi_{SNP}\beta_{SNP} + (1 - \varphi_{hnf})\beta_{host} \tag{9}$$

where, $\varphi_{hnf} = \varphi_{SNP} + \varphi_{NEPCM}$ Subscript "SNP" shows simple nanoparticles, those without any phase change, MWCNTS. Subscript "NEPCM" explains the nano-encapsulated phase change materials. Thus, a hybrid nanofluid would be a contribution of both simple nanoparticles and nano-encapsulated phase change materials inside a base fluid with a "host" subscript. The dynamic viscosity and the thermal conductivity of the hybrid nanofluid are specified regarding upgraded Brinkmann and Maxwell equations, respectively [36]:

$$\frac{\mu_{hnf}}{\mu_{host}} = \frac{1}{(1 - \varphi_{SNP} - \varphi_{NEPCM})^{2.5}} \tag{10}$$

$$\frac{k_{hnf}}{k_{host}} = \frac{\frac{(\varphi_{SNP}k_{SNP} + \varphi_{NEPCM}k_{NEPCM})}{\varphi_{hnf}} + 2k_{bf} + 2(\varphi_{SNP}k_{SNP} + \varphi_{NEPCM}k_{NEPCM}) - 2\varphi_{hnf}k_{bf}}{\frac{(\varphi_{SNP}k_{SNP} + \varphi_{NEPCM}k_{NEPCM})}{\varphi_{hnf}} + 2k_{bf} - 2(\varphi_{SNP}k_{SNP} + \varphi_{NEPCM}k_{NEPCM}) - 2\varphi_{hnf}k_{bf}} \tag{11}$$

To make the comparative results, the governing equations regarding the boundary conditions should be scaled into their dimensionless form. To do it, the following parameters have been considered:

$$(X, Y) = \frac{(x, y)}{L}, U = \frac{uL}{\alpha_{host}}, V = \frac{vL}{\alpha_{host}}, P = \frac{pL^2}{\rho_{host}\alpha_{host}^2}, \theta = \frac{T - T_c}{T_h - T_c}, \theta_f = \frac{T_f - T_c}{(T_h - T_c)} \tag{12}$$

Utilizing equation (12), governing equations (1)–(4) in their dimensionless form are obtained as:

$$\frac{\partial U}{\partial X} + \frac{\partial V}{\partial Y} = 0 \tag{13}$$

$$\frac{\rho_{hnf}}{\rho_{host}}\left(U\frac{\partial U}{\partial X} + V\frac{\partial U}{\partial Y}\right) = -\frac{\partial P}{\partial X} + \frac{\mu_{hnf}}{\mu_{host}}Pr\left(\frac{\partial^2 U}{\partial X^2} + \frac{\partial^2 U}{\partial Y^2}\right) \tag{14}$$

$$\frac{\rho_{hnf}}{\rho_{host}}\left(U\frac{\partial V}{\partial X} + V\frac{\partial V}{\partial Y}\right) = -\frac{\partial P}{\partial Y} + \frac{\mu_{hnf}}{\mu_{host}}Pr\left(\frac{\partial^2 V}{\partial X^2} + \frac{\partial^2 V}{\partial Y^2}\right) + \frac{(\rho\beta)_{hnf}}{(\rho\beta)_{host}}RaPr\theta \tag{15}$$

$$\frac{(\rho C_p)_{hnf}}{(\rho C_p)_{host}}\left(U\frac{\partial \theta}{\partial x} + V\frac{\partial \theta}{\partial y}\right) = \frac{k_{hnf}}{k_{host}}\left(\frac{\partial^2 \theta}{\partial X^2} + \frac{\partial^2 \theta}{\partial Y^2}\right) \tag{16}$$

The well-known dimensionless numbers, Rayleigh (*Ra*) and Prandtl (*Pr*) numbers appeared in equation (14), and (15), and are defined as:

$$Ra = \frac{g\rho_{host}\beta_{host}\Delta TL^3}{\alpha_{host}\mu_{host}}, Pr = \frac{\mu_{host}}{\rho_{host}\alpha_{host}} \tag{17}$$

In equation (16),

$$\frac{(\rho C_p)_{hnf}}{(\rho C_p)_{host}} = Cr \tag{18}$$

where

$$Cr = \frac{(\rho C_p)_{hnf}}{(\rho C_p)_{host}} = (1-\varphi_{hnf}) + \varphi_{SNP}\lambda_{SNP} + \varphi_{NEPCM}\lambda_{NEPCM} + \frac{\varphi_{NEPCM}}{\delta\, Ste} f \tag{19}$$

Cr provides the heat capacity ratio of the suspension to the sensible heat capacity of the host fluid. Moreover, the variables, including the heat capacity ratio, defined as λ (both of SNP and NEPCM), the dimensionless phase transition range symbolized by δ, and the Stefan number, indicated as *Ste*, are all specified as follows:

$$\lambda_{SNP} = \left(\frac{(\rho C_p)_{SNP}}{(\rho C_p)_{host}}\right), \lambda_{NEPCM} = \frac{(Cp_{core,l} + \imath Cp_{shell})\rho_{core}\rho_{shell}}{(\rho Cp)_{host}(\rho_{sell} + \imath\rho_{core})}, \delta = \frac{T_{Mr}}{\Delta T},$$
$$Ste = \frac{(\rho Cp)_{host}\Delta T(\rho_{sell} + \imath\rho_{core})}{\alpha_{host}(h_{sf}\rho_{core}\rho_{sell})} \tag{20}$$

Also, *f*, in equation (19), the dimensionless fusion function, can be defined as:

$$f = \frac{\pi}{2}\sin\left[\left(\frac{\delta}{2} + \theta - \theta_m\right)\frac{\pi}{\delta}\right] \times \begin{cases} 0 & \theta < \theta_m - \delta/2 \\ 1 & \theta_m - \delta/2 < \theta < \theta_f + \delta/2 \\ 0 & \theta > \theta_m + \delta/2 \end{cases} \tag{21}$$

where θ_f, the dimensionless fusion temperature, is:

$$\theta_f = \frac{T_m - T_c}{\Delta T} \tag{22}$$

finally, the term $\frac{\beta_{hnf}}{\beta_{host}}$ can be written as:

$$\frac{\beta_{hnf}}{\beta_{host}} = \varphi_{NEPCM}\frac{\beta_{NEPCM}}{\beta_{host}} + \varphi_{SNP}\frac{\beta_{SNP}}{\beta_{host}} + (1-\varphi_{hnf}) \tag{23}$$

Since the nanoparticles' thermal expansion (β_{SNP} and β_{NEPCM}) is much smaller than the host fluid (β_{host}), hence, the first and the second terms on the right side of equation (23) tend to be zero (→0), and can be neglected. Thus, equation (23) is diminished to the following form:

$$\frac{\beta_{hnf}}{\beta_{host}} = (1-\varphi_{hnf}) \tag{24}$$

Regarding the boundary conditions, the set of equation (5) can be expressed in their dimensionless form in the set of equation (25):

$$X = 0 \;\rightarrow\; \theta = 1, U = V = 0 \tag{25-a}$$

$$X = 1 \;\rightarrow\; \theta = 0, U = V = 0 \tag{25-b}$$

$$\left.\frac{\partial\theta}{\partial Y}\right|_{Y=0} = 0, U = V = 0 \tag{25-c}$$

$$\left.\frac{\partial\theta}{\partial Y}\right|_{Y=1} = 0, U = V = 0 \tag{25-d}$$

The dimensionless form of equation (6), total entropy generation, can be written as follows [40]:

$$S_T = S_\theta + S_\psi = \frac{k_{hnf}}{k_{host}}\left(\left(\frac{\partial\theta}{\partial X}\right)^2 + \left(\frac{\partial\theta}{\partial Y}\right)^2\right) + \chi_0\frac{\mu_{hnf}}{\mu_{host}}\left(2\left(\frac{\partial U}{\partial X}\right)^2 + 2\left(\frac{\partial V}{\partial Y}\right)^2 + \left(\frac{\partial U}{\partial Y} + \frac{\partial V}{\partial X}\right)^2\right) \tag{26}$$

χ_0 in the above relation is the irreversibility parameter. To denote it:

$$\chi_0 = \frac{\mu_{\text{host}} T_0}{k_{\text{host}}} \left(\frac{\alpha_{\text{host}}}{\mathrm{L}(T_h - T_c)} \right)^2 \tag{27}$$

$$Entropy = \frac{\oint S_T dA}{A} \tag{28}$$

Considering equation (26), the ratio of heat transfer term (S_θ) to total entropy generation (S_T) can be led to Bejan number [41]:

$$Be = \frac{S_\theta}{S_T} = \frac{\frac{k_{hnf}}{k_{host}} \left(\left(\frac{\partial \theta}{\partial X} \right)^2 + \left(\frac{\partial \theta}{\partial Y} \right)^2 \right)}{\frac{k_{hnf}}{k_{host}} \left(\left(\frac{\partial \theta}{\partial X} \right)^2 + \left(\frac{\partial \theta}{\partial Y} \right)^2 \right) + \chi_0 \frac{\mu_{hnf}}{\mu_{host}} \left(2 \left(\frac{\partial U}{\partial X} \right)^2 + 2 \left(\frac{\partial V}{\partial Y} \right)^2 + \left(\frac{\partial U}{\partial Y} + \frac{\partial V}{\partial X} \right)^2 \right)} \tag{29}$$

Where, the average Bejan number throughout the enclosure is defined as:

$$Be_{Avg} = \frac{\oint Be \, dA}{A} \tag{30}$$

Importantly, through $Be_{\text{AVG}} < 0.5$ and $Be_{\text{AVG}} > 0.5$, irreversibility of the friction term and the heat transfer term drive the total entropy generation, respectively.

In addition, the dimensionless streamline (ω) can be introduced as:

$$\nabla^2 \omega = \left(\frac{\partial U}{\partial Y} - \frac{\partial V}{\partial X} \right) \tag{31}$$

in which $U = \partial\omega/\partial Y$, and $V = -\partial\omega/\partial X$. It is worth noting that $\omega = 0$ was applied on the enclosure walls as referred to in Refs. [42,43]. As a key dimensionless number in the heat transfer problems, the Nusselt number is defined on the left hot wall of the enclosure:

$$Nu_{\text{Local}} = -\frac{\mathrm{k_{hnf}}}{\mathrm{k_{host}}} \left(\frac{\partial \theta}{\partial \mathrm{X}} \right)_{\text{on x=0}} \tag{32}$$

additionally, the average Nusselt number associated with the hot wall can be formulated as follows:

$$Nu_{\text{Avg}} = \int_0^1 -\frac{\mathrm{k_{hnf}}}{\mathrm{k_{host}}} \left(\frac{\partial \theta}{\partial \mathrm{X}} \right)_{\text{on x=0}} \mathrm{dY} \tag{33}$$

The results of the present study can be applied in various engineering fields, such as heat rejection from electronic devices, thermal energy storage systems, and heat exchangers, by considering the laminar natural convection heat transfer of MWCNTs-NEPCMs-Water hybrid nanofluid. It is worth noting that the nano capsules in the hybrid NEPCM suspension improve the heat capacity, while the MWCNTs enhance the thermal conductivity. This results in a suspension with better overall heat capacity and thermal conductivity compared to the host fluid (water).

3. Numerical method and grid independence

In the current investigation, the partial differential equations, including continuity, momentum, and energy, as well as their associated boundary conditions, are formulated in a weak form. Subsequently, the Galerkin finite element method (GFEM) was applied to integrate these equations. Additionally, to transform the governing equations into a set of algebraic equations, a triangular grid style was selected for discretization. The momentum equations were discretized using a scheme that achieved second-order accuracy, ensuring a higher level of precision in the numerical calculations. On the other hand, a linear discretization scheme was employed for the homogeneous hybrid nanofluid, providing a simpler and more straightforward approach to handle the fluid properties. By considering the governing equations as fully coupled, the Newton method was utilized iteratively to solve them. The calculations were iterated until the residuals decreased to a value smaller than 10^{-6}. Further information regarding the numerical approach employed in this study can be addressed in Ref. [44], and [45].

To employ triangular elements, the computations were iterated across five distinct grid sizes, as outlined in Table 2. The

Table 2
Impact of mesh elements on average Nusselt number and total entropy generation for Ra = 10^5, Pr = 6.2, Ste = 0.3, $\chi_0 = 10^{-4}$, $\varphi_{hnf} = 0.05$ ($\varphi_{NEPCM} = 0.025$, $\varphi_{SNP} = 0.025$), $\theta_f = 0.3$.

Case No.	Mesh quality	Mesh quantity (Overall number of Elements)	Nu_t	*Err* (%)	S_T	*Err* (%)
1	Normal	1626	5.3521	0.18	26.0855	0.41
2	Fine	2650	5.3617	1.02	25.9800	0.40
3	Finer	6830	5.3077	0.017	26.0843	0.22
4	**Extra Fine**	**17600**	**5.3086**	**0.03**	**26.1417**	**0.048**
5	Extremely fine	26856	5.3070	–	26.1542	–

*Bold row shows the selected mesh size for computations.

determination of average Nusselt number and total entropy generation values was carried out for various grid sizes. Notably, for the mesh size of 17600 (Case 4), minimal variations, on the order of 10^{-2}, in average Nusselt and total entropy generation, were observed. Besides Table 2, Fig. 3 depict the values of the velocity components (U and V) in the mid-plane of the enclosure across the five mentioned grids, where $-0.5 \leq X \leq 0.5$ and $Y = 0$. As seen, the curves corresponding to cases 4 and 5 are so closely aligned. Hence, the obtained results approve those that occurred in Table 2. Therefore, all the results would be derived using a computational grid size of 17600 (Case 4)The views of the selected grid size (Case 4) have been shown in Fig. 4 as well. As a defined rule, the triangular elements have a high density around the corners and near the walls.

4. Validation

To ensure the qualification of the present computational code, we have considered two valid studies and compared the code with the results obtained from them. The first is related to Kahveci's study [38]. Kahveci [38] has explored the heat transfer process in water-based nanofluids. The study focuses on the impact of buoyancy on this heat transfer phenomenon within a specially designed container. The nanoparticles applied in the investigation [38] were Cu, Ag, CuO, Al_2O_3, and TiO_2. The comparison has been made for a 45^o tilted enclosure with $Ra = 10^4$ and a volume fraction of $\varphi = 0.2$. Fig. 5 shows the isotherm contours for Water—Cu nanofluid. The obtained patterns agree completely. Besides, the results of the present code for heat transfer of hybrid nanofluids were compared with the studies of Chabani et al. [46] and Mebarek-Oudina et al. [28] and found in good agreement.

The second validation is among the most closely related works to the current study. The heat transfer properties of NEPCM-Water, a nanofluid within a square enclosure, were meticulously examined by Ghalambaz et al. [45]. In their study [47], left and right walls had a specified temperature difference, while the horizontal ones were fully insulated. Fig. 4 depicts the chosen outputs for $\theta_f = 0.3$. The first row in Fig. 6 is related to the heat capacity ratio parameter (Cr) contours. As seen, the provided ribbon on the left (Ghalambaz et al. [45]) and the right Figures (Present study) have the same pattern, where the phase change process regarding the nano-capsules has happened. The second row in Fig. 4 reveals streamlined patterns obtained from the mentioned study [45] (left side) and the present work (right side). To better distinguish the provided comparison, We have considered the streamlines with the lower density against those obtained by Ref. [47]. According to the provided results, an appropriate accuracy between the studies has been depicted.

5. Results and discussions

The interest parameters and numbers in the present study include Rayleigh number (Ra), the volume fraction of the nanoparticles (φ_{SNP} and φ_{NEPCM}), and fusion temperature (θ_f). The default values and the specified range of the mentioned numbers/parameters are listed in Table 3. The others have been considered constant as $Pr = 6.2$, $Ste = 0.3$, $\chi_0 = 10^{-4}$, and $d = 0.05$. Local and average Nusselt numbers, total entropy generation, contours (isotherm, Cr, and entropy generation), and streamlines make up the results and discussion atmosphere.

Fig. 7 depicts the variation in local Nusselt number (Nu_L) along the hot wall for different Rayleigh numbers (Ra). It is observed that as the Rayleigh number increases from $Ra = 10^3$ to $Ra = 10^5$, there is a significant enhancement in the local Nusselt number. With the increase in Rayleigh number, buoyancy forces intensify, leading to a dominance of convective heat transfer mechanisms. This stronger buoyancy force drives a more vigorous flow of the hybrid nanofluid, effectively reducing the thermal equilibrium near the hot wall. As

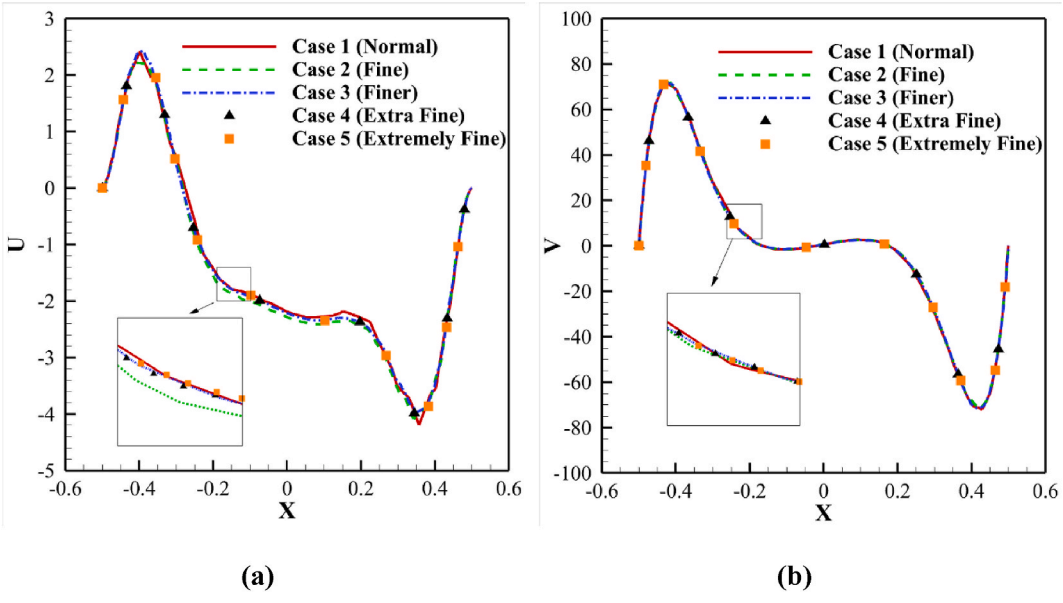

Fig. 3. (a) Horizontal velocity and (b) vertical velocity, at mid-plane of the enclosure at $Y = 0$ for various evaluated meshes.

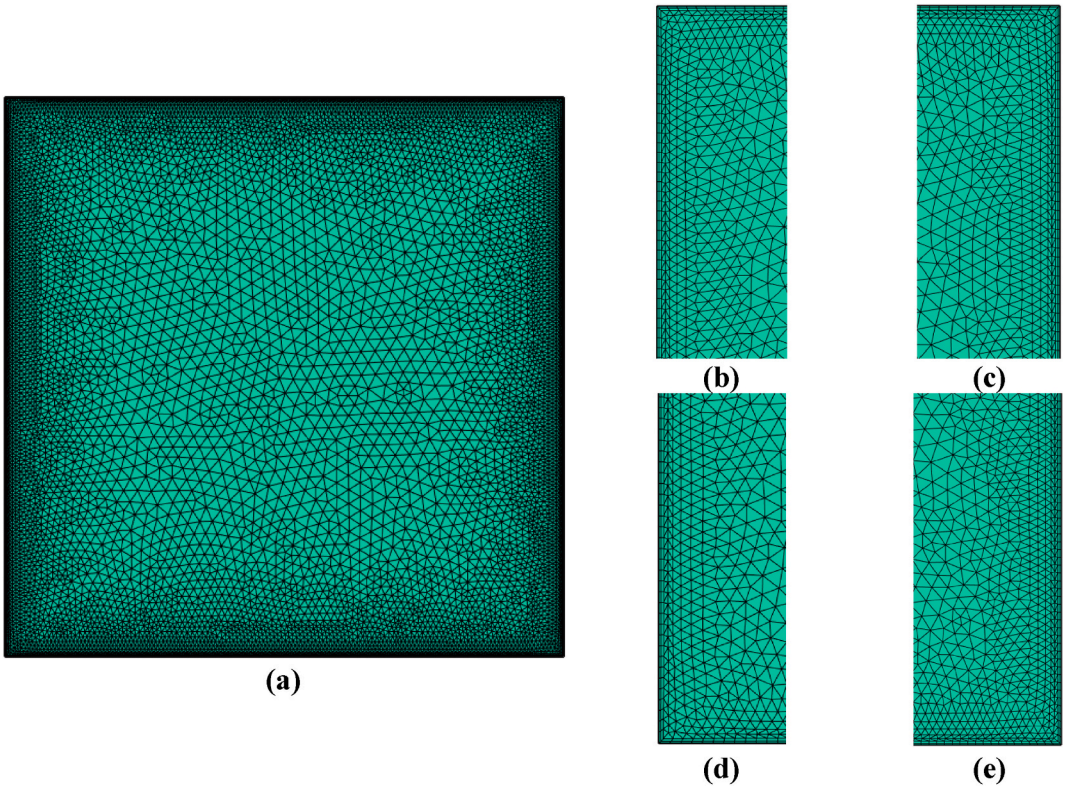

Fig. 4. The views of the chosen mesh: (a) Overall view, (b) Left- Top corner, (c) Right-Top Corner, (d) Left-Bottom corner, and (e) Right- Bottom corner.

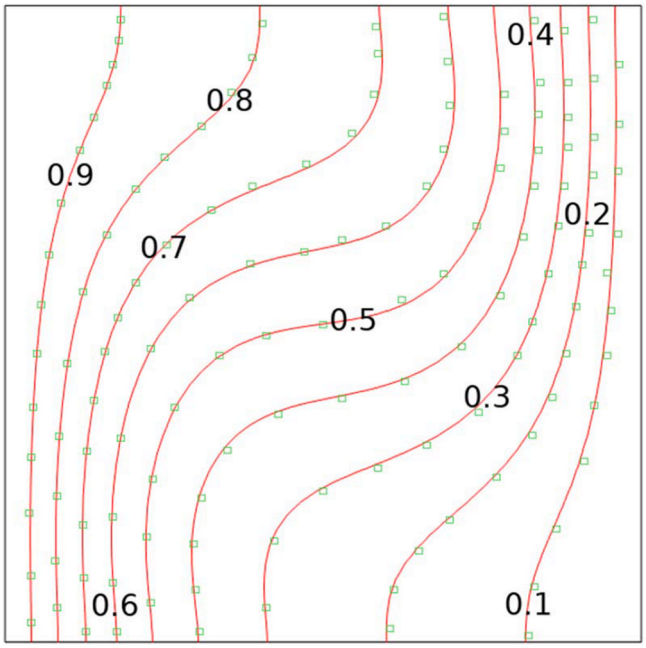

Fig. 5. A comparison between the obtained isotherm contours, (symbols) Kahveci results [38], and (continuous line) the present study, for Ra $= 10^4$, $\varphi = 0.2$ (copper nanoparticles) and a 45° tilted angle.

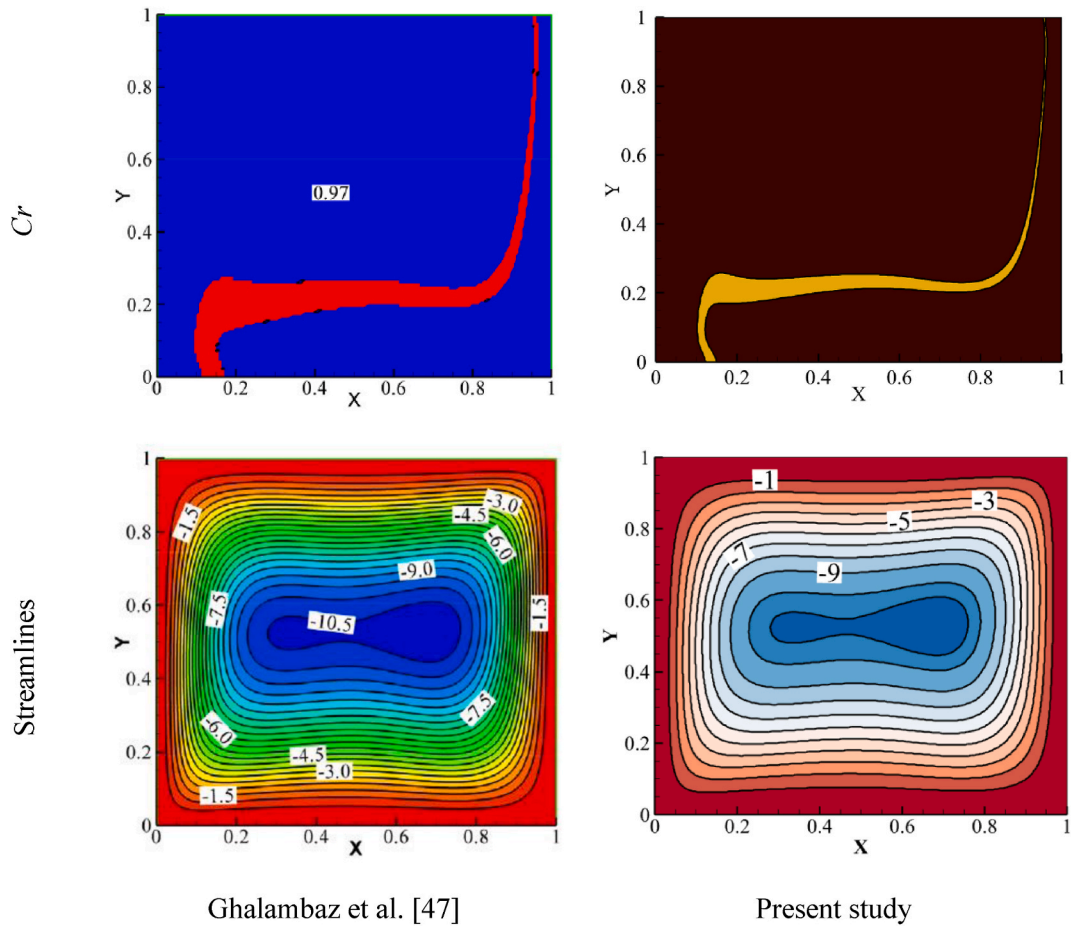

Fig. 6. Comparisons between the present study and the results obtained by Ghalambaz et al. [47] with permission from Elsevier, (First row) heat capacity ratio parameter (*Cr*), and (Second row) Streamlines.

Table 3
The dimensionless numbers/parameters probed in the results and discussion section.

Dimensionless number/parameter	Default value	Lower bound	Upper bound
Rayleigh number (Ra)	10^5	10^3	10^5
The volume fraction of the nanoparticles ($\varphi_{SNP} + \varphi_{NEPCM}$)	0.025/0.025	0/0	0.025/0.025
Fusion temperature (θ_f)	0.3	0.1	0.5

a result, more pronounced thermal gradients are established in this region. The maximum value of the local Nusselt number (Nu_L) regarding curve $Ra = 10^6$ is over 6 times larger than one obtained via curve $Ra = 10^3$. In each curve, the referred maximum value of the local Nusselt number (Nu_L) occurs in the bottom area of the enclosure, where the cold hybrid nanofluid meets the hot wall for the first time. Climbing the hybrid nanofluid in the vicinity of the hot wall gets the heat from the mentioned wall so that the most thermal equilibrium (the weakest gradients) can occur at the top area of the hot wall.

Isotherm, heat capacity ratio parameter (*Cr*), and entropy generation contours, as well as streamlines for the specified values of Rayleigh number (Ra), are depicted in Fig. 8. According to the first row, the isotherm contours for the minimum value of Rayleigh number ($Ra = 10^3$) are so smooth. As the Rayleigh number (Ra) increases, the degree of distortion experienced by the isotherms also intensifies so that the most ones can be observed in $Ra = 10^5$. It is worth noting that the intensity of isotherm layers close to the hot wall becomes greater when the Rayleigh number (*Ra*) is increased. Hence, the obtained results in the first row completely agree with those provided in Fig. 7. According to the second row, the phase change process of the hybrid nanofluid happens on the yellow ribbons, where the maximum value of the heat capacity ratio parameters (*Cr*) is obtained. Depending on the isotherm contours pattern, for the lowest value of Rayleigh number ($Ra = 10^3$), the obtained ribbon has a uniform thickness and is placed in the central area of the enclosure. An increase in Rayleigh number (Ra) leads to extending the mentioned ribbon. It gets a narrow and thick shape close to the cold and hot walls, respectively. Actually, the minimum fusion is close to the cold wall. However, the maximum one can be created on the bottom area, near the left hot wall. When the Rayleigh number (*Ra*) is raised, entropy generation is also increased (see the third

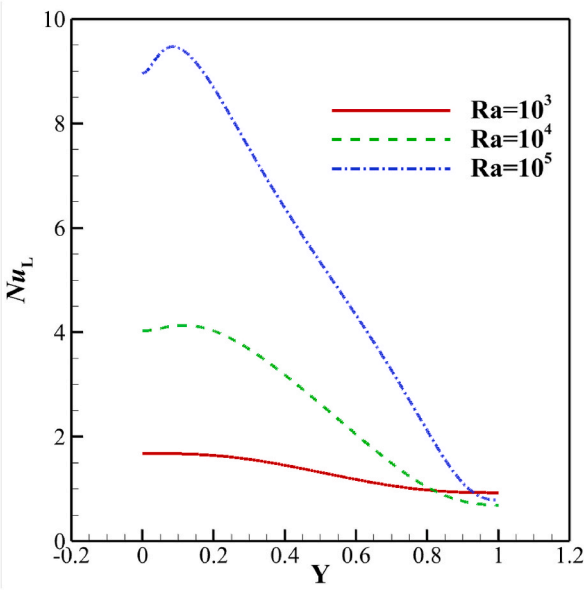

Fig. 7. Local Nusselt number as a function of different values of Rayleigh number.

row). As referred, a robust fluid flow has higher velocity and stronger thermal gradients. Hence, entropy generation, especially near the vertical walls, has the maximum values. The fourth row shows the streamlines for the mentioned values of the Rayleigh number (*Ra*). Those created at the center area of the enclosure are the weak circles, while the strongest ones are configured toward the outer layers. For the lowest value of Rayleigh number ($Ra = 10^3$), the obtained streamlines are symmetrical compared to the X and Y axes. By raising the Rayleigh number (Ra), a bipolar tendency can be observed gradually.

Fig. 9 reveals the local Nusselt number (Nu_L) on the hot wall for different values of the dimensionless fusion temperature parameter (θ_f). The general pattern for the obtained curves is approximately the same. Moreover, apart from the bottom area of the hot wall, variation in the value of the dimensionless fusion temperature (θ_f) has not made any significant change in the local Nusselt number (Nu_L). Indeed, the melting process of the hybrid nanofluid occurs at a constant temperature without any sensible effect on the thermal gradients. Thus, it is concluded that during the phase change process, the latent thermal energy aspect is dominant, whether the fusion temperature has a low or high value.

The Set of the contours and streamlines for different values of the dimensionless fusion temperature (θ_f) are shown in Fig. 10. In accordance with the obtained results in Fig. 9, and despite increasing the dimensionless fusion temperature (θ_f), there is no significant effect within the first, third, and fourth rows in Fig. 10. As referred, isotherm and entropy generation contours as well as streamlines are a function of the sensible thermal energy aspect. However, an obvious change can be observed in the second row, the obtained patterns for the heat capacity ratio parameter (*Cr*). Generally, when the dimensionless fusion temperature (θ_f) has a low value ($\theta_f = 0.1$), the yellow ribbon remains near the cold wall. Unlike when the mentioned parameter is high ($\theta_f = 0.5$), the yellow ribbon is extended to the hot wall. In other words, by a low ($\theta_f = 0.1$) and high ($\theta_f = 0.5$) value of the dimensionless fusion temperature (θ_f), the melting conditions are satisfied near the cold and hot walls, respectively.

To understand the synergistic effect through the applied nanoparticles in the present hybrid nanofluid, Fig. 11 has been provided. The relationship between the average Nusselt number (Nu_{AVG}) and the volume fraction of the nano-encapsulated phase change material (NEPCM) is depicted in Fig. 11(a). This graph illustrates how the Nu_{AVG} changes as the NEPCM volume fraction varies. Each curve has been provided for the specified value of simple nanoparticle (SNP) volume fraction. The absence of simple nanoparticles ($\varphi_{SNP} = 0$, continuous red curve) does not yield any noticeable effect on the average Nusselt number (Nu_{AVG}) as the volume fraction of NEPCM is increased. When the suspension contains the simple nanoparticles (SNP) as well, the heat transfer rate is augmented (see green and blue curves). In this case, appending the NEPCMs to the suspension enhances the heat transfer rate significantly; so that the maximum value of the average Nusselt number (Nu_{AVG}) is related to $\varphi_{\mathbf{SNP}} = 0.025$, and $\varphi_{\mathbf{NEPCM}} = 0.025$, about 13 % enhancement than the host fluid. According to Fig. 11(b), total entropy generation is affected by SNP, and NEPCM volume fraction. An enclosure containing only NEPCMs causes an apparent decrease in total entropy generation, even less than the pure water fluid flow. Because of the changing cores of NEPCM, a higher value of NEPCM volume fraction involves a larger portion of the thermal gradients; so, entropy generation in the presence of maximum NEPCM volume fraction, 0.025, is reduced by about 10 % than the host fluid, 22.8 versus 25.2. On the other hand, a higher value of SNP volume fraction ($\varphi_{\mathbf{SNP}}$) increases total entropy generation in the enclosure. MWCNTs have no phase-changing process and remain in the solid phase as long as the host fluid is contained. Hence, when the enclosure is empty of NEPCM, adding SNP to the host fluid grows up the thermal, and frictional aspects, by more than 6 % than the host fluid. By considering the hybrid nanofluid ($\varphi_{\mathbf{SNP}} \neq 0$ and script phiEPCM$\neq$0), the reduction slope is continued for the green dashed and blue dashed-dot curves. Indeed, the existence of the NEPCMs in the enclosure always has a damping effect on the total entropy generation.

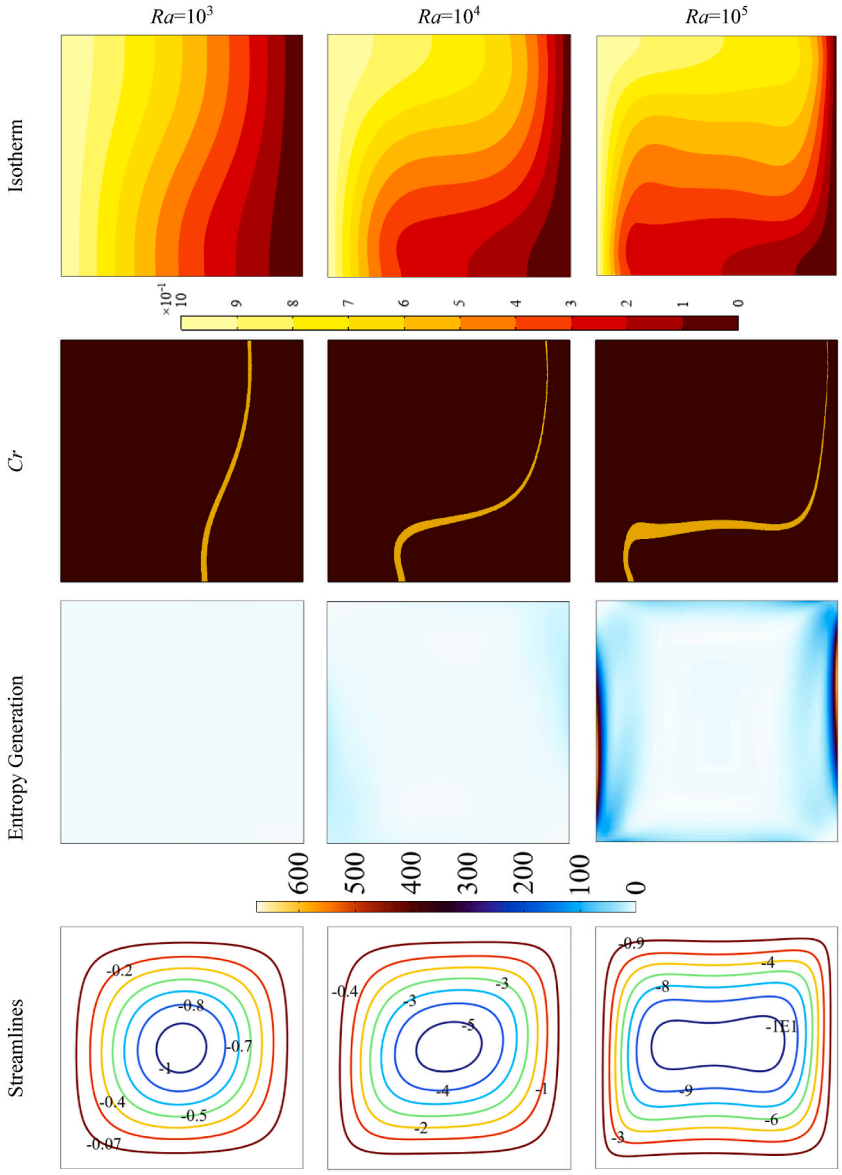

Fig. 8. Isotherm and Cr contours, entropy generation, and streamlines for Ra = 10^3, 10^4, and 10^5.

Anyway, less than 5 % of the total entropy generation occurs than the host water fluid. Since MWCNTs as SNP create a high value of the heat transfer rate, and nano-encapsulated phase change materials (NEPCM) have a reduction effect on the total entropy generation, the synergistic phenomena can be so clear in the mentioned enclosure.

Table 4 depicts the effects of Rayleigh number (Ra) and nanoparticles volume fraction ($\varphi_{\mathbf{hnf}}$) on average Bejan number (Be_{AVG}). According to the obtained results, increasing Rayleigh number (Ra) causes average Bejan number (Be_{AVG}) to be deteriorated. As referred, when Rayleigh number (Ra) increases, the hybrid nanofluid buoyancy forces are augmented everywhere within the enclosure. On the one hand, the thermal gradients are flourished and consequently, heat transfer rate enhances. On the other hand, the hybrid nanofluid gets more velocity which leads to more intensive friction in the enclosure. More growing up the friction entropy generation (S_ψ) against the heat transfer entropy generation (S_θ) is the reason why average Bejan number (Be_{AVG}) becomes a reduction function than increasing Rayleigh number (Ra).

As seen in Table 4, impression of the nanoparticles volume fraction ($\varphi_{\mathbf{hnf}}$) on average Bejan number (Be_{AVG}) is so slightly. Positive effect of adding the nanoparticles on the thermal gradients has already been shown in Fig. 11(a). Hence, an approximately constant value of Bejan number (Be_{AVG}) means that both of the heat transfer entropy generation (S_θ) and the total entropy generation (S_{T}) have equally been enhanced.

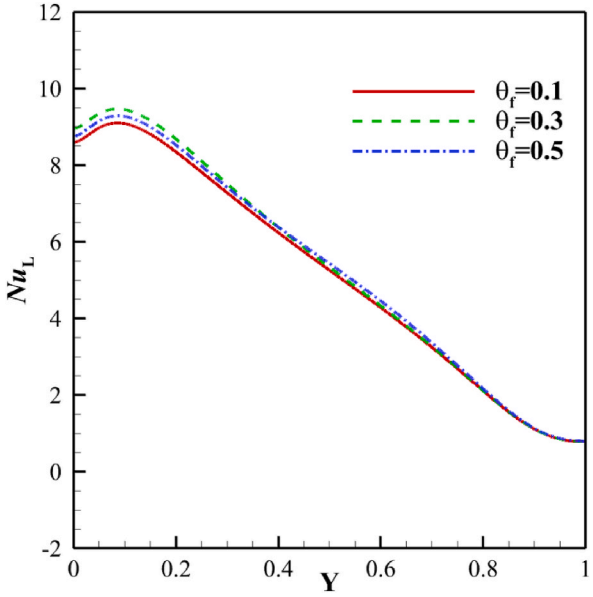

Fig. 9. Local Nusselt number as a function of different values of fusion temperature (θ_f).

6. Neural network study

Here, the neural networks (NNs), as part of machine learning approaches, are utilized to further study the present physical model. The neural networks are employed to learn the underlying physics of a heat transfer of hybrid NEPCM suspensions in an enclosure. A dataset of 1000 records was created by numerically solving the model for a random set of control parameters. The range of control parameters was adopted as $10^3<Ra<10^5$, $0<\varphi<0.05$, $0.3<\theta_f<0.7$. The dataset consists of 1000 records, each comprising input parameters and their corresponding physical output (Nu_{Avg}). These records encapsulate the essential dynamics of a physical model, presenting a challenging yet insightful opportunity to examine the model's behavior through a neural network lens. The objective is to develop an NN model capable of accurately predicting the output based on unseen input parameters, thereby unraveling the physics governing the model.

The methodology begins with preprocessing the dataset to facilitate efficient learning. The dataset is divided into training, testing, and validation sets, with a 70-15-15 split between the training, testing, and validation sets. This division ensures that the model is exposed to a wide variety of scenarios during training while retaining a significant portion of data for unbiased evaluation. Furthermore, feature scaling is applied to normalize the input and output data, enhancing the NN's ability to converge to an optimal solution more swiftly and reliably [48,49].

The architecture of the neural network is thoughtfully designed to capture the complexity of the physical model. It consists of an input layer, followed by multiple dense layers with sigmoid activation functions, and culminates in an output layer that predicts the physical output [50,51]. Fig. 12 displays a schematic representation of NN. The choice of sigmoid activation functions is strategic, aiming to introduce non-linearity into the model, enabling it to learn complex relationships between the input and output parameters. Dropout layers are considered but ultimately not included in the final architecture to maintain model simplicity and focus on understanding the direct mappings from inputs to outputs.

Training the model involves a meticulous process of optimization and validation. The Adam optimizer [52] is chosen for its efficiency in handling sparse gradients and its adaptability in adjusting the learning rate, making it well-suited for our dataset. The model has trained over a thousand epochs, with a batch size of four, allowing for a granular update of the model's weights, which is crucial for learning the nuanced behaviors of the physical model. A model checkpoint callback ensures that the model with the best validation loss is saved, providing a reliable snapshot of the most accurate model during training.

The model's performance is evaluated twofold, focusing on validation and testing datasets. The validation dataset plays a critical role in tuning the model during training, while the testing dataset offers an unbiased assessment of the model's predictive capabilities. Fig. 13 depicts the loss function values during the training process. The lowest validation loss function was computed as 0.228×10^{-3} with the corresponding training loss function value of 0.230×10^{-3}. The results are promising, showing that the neural network can accurately predict the physical outputs from the inputs with minimal loss. This accuracy is a testament to the model's ability to learn the underlying physics of the model.

Visualization of the training history and predictions further illustrates the model's performance, as depicted in Fig. 13. Loss plots reveal the convergence of the model over epochs, highlighting the reduction in training and validation loss. Fig. 14 presents a scatter plot comparing predicted data with actual observations. Comparing the actual and predicted outputs for the testing dataset demonstrates the model's predictive accuracy, with a clear linear relationship between the two, indicating high fidelity in the model's predictions.

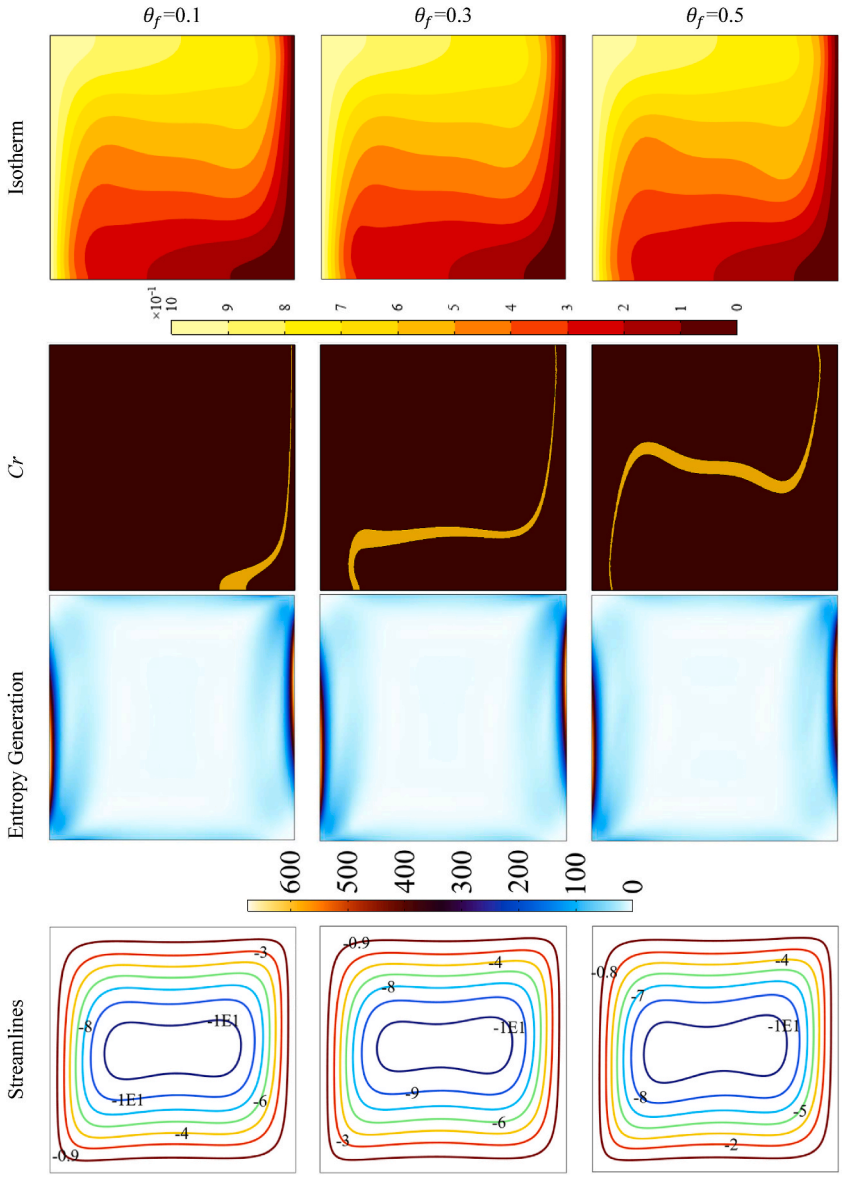

Fig. 10. Isotherm and *Cr* contours, entropy generation, and streamlines for three values of the dimensionless fusion temperature (θ_f).

The trained model can be used for optimization of the Nu_{Avg} by optimization methods such as response surface methodology [46] as the trained NN can mathematically map the relationship between control parameters and Nu_{Avg}. Here, the trained model was utilized to plot the impact of model features on the heat transfer rate (Nu_{Avg}). Fig. 15 shows the influence of hybrid nanoparticle concentration and fusion temperature on heat transfer rate. This image is produced by computing more than 4000 points. Each point indicates a simulation performed by the trained neural network. The neural network produced this map in seconds, while each simulation case takes a few minutes to be computed using the finite element method discussed in section 3. Thus, producing such contour using FEM requires very costly computations, while the trained NN produces the outcomes very quickly.

As seen in Fig. 15, generally, an increase in hybrid nanoparticle concentration increases the heat transfer rate. For low concentrations of nanoparticles, an optimum fusion temperature of about $\theta_f = 0.5$ can be observed. However, as the concentration increases, the fusion temperature $\theta_f = 0.9$ provides the highest heat transfer rate. This change of physical behavior by the concentration increase is attributed to the dual nature of hybrid nanoparticles and the combined heat transfer impact of NEPCM particles and MWCNTs on the heat transfer rate. Fig. 16 shows the influence of Rayleigh number and fusion temperature on the heat transfer rate. This figure demonstrates that an increase in Rayleigh number and fusion temperature would improve the heat transfer rate. The impact of the variation of fusion temperature on heat transfer rate is almost linear, while the Rayleigh number shows a non-linear influence.

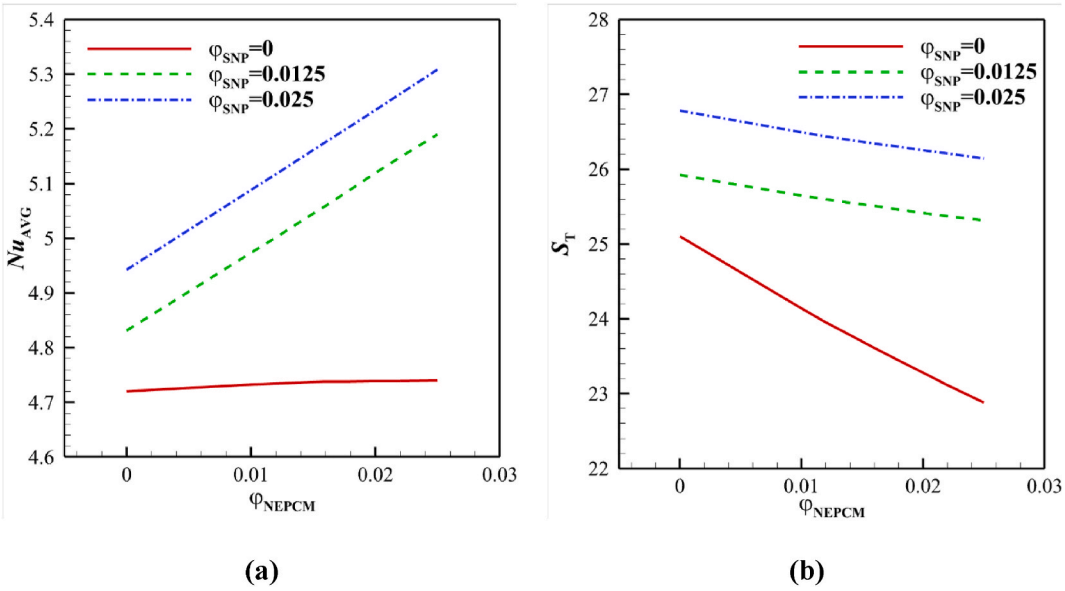

Fig. 11. (a) Average Nusselt number, and (b) Total entropy generation, as a function of nano-encapsulated phase change materials volume fraction (φ_{NEPCM}) for different values of simple nanoparticle volume fractions (φ_{SNP}).

Table 4
Evaluation of average Bejan number (Be_{AVG}) in different values of Rayleigh number (Ra), and volume fraction of nanoparticles (φ_{hnf}) for default values shown in Table 3.

Parameter	Rayleigh Number (Ra)			Nanoparticles Volume Fraction (φ_{hnf})		
Range of parameters	10^3	10^4	10^5	0	0.0125	0.025
Average Bejan number (Be_{AVG})	0.98	0.67	0.29	0.28	0.29	0.29

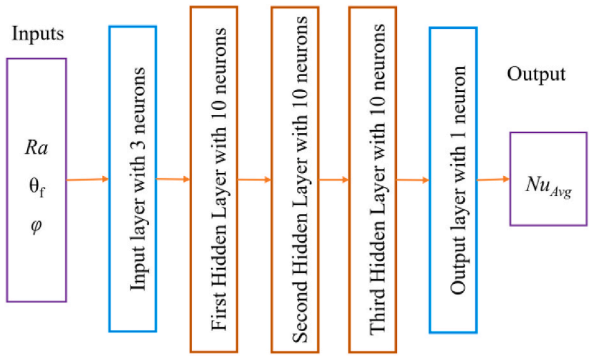

Fig. 12. The structure of the employed NN. The number of neurons in the input and output layers matches the input parameters.

7. Conclusion

The present study was provided to find the synergistic impression of MWCNTs, and NEPCMs nanoparticles dispersed in the host water within the square enclosure. A dataset of 1000 records from a simulated numerical model was created to train a neural network. The trained neural network was used to analyze further the impact of control parameters on heat transfer rate. The results are reported based on the dimensionless numbers and parameters in the form of curves, contours, and streamlines, which were discussed in detail. The most important ones are listed below:

I) The heat transfer rate in the bottom area of the hot wall via $Ra = 10^6$ can reach over six times the related value provided through $Ra = 10^3$. Rayleigh number promotes the buoyancy force, which causes the thermal gradients to grow. Hence, the isotherm and, consequently, Cr contours and streamlines were extended inside the enclosure via a higher value of Rayleigh number. Besides, the entropy generation was significantly increased.

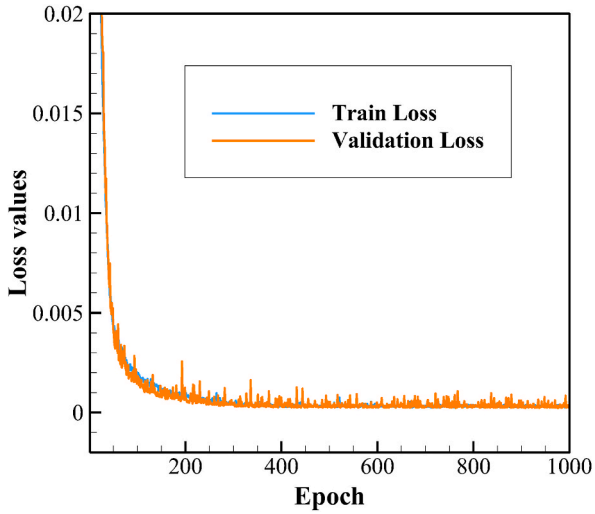

Fig. 13. The values of the training and validation loss functions during the training process.

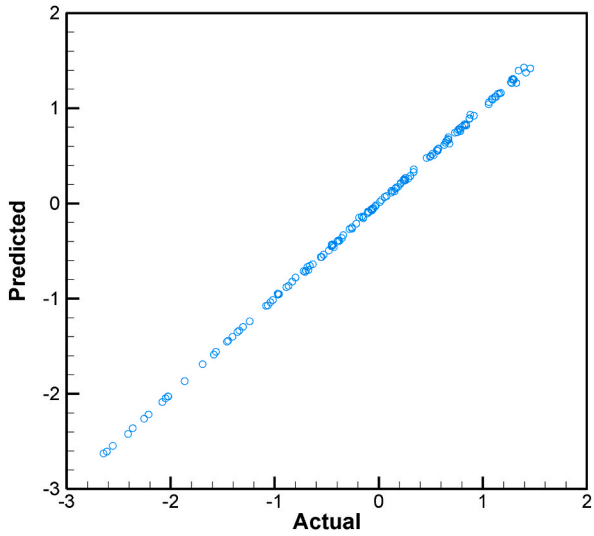

Fig. 14. The comparison of actual and predicted data for the test dataset. The data are aligned about a line with 45-degree slope indicating that the predicted data are close to the actual data.

II) Non-dimensional fusion temperature parameter (θ_f), which is mainly controlled by the boundary condition temperature, could notably shift the location of phase change. However, altering the value of the aforementioned parameter (θ_f) does not yield any noteworthy impact on the isotherm (thermal gradients), entropy generation contours, and streamlines. Variation of the fusion temperature parameters (θ_f), causes hybrid nanofluid melting conditions to be satisfied near the cold or hot walls, depending on the value of non-dimensional fusion temperature.

III) The absence of each type of nanoparticle (NEPCM or MWCNTs) disturbs the synergistic impression. In the case of the host water, including NECPMs, there would not be any evident increase in the heat transfer rate. Further, by using MWCNTs alone, besides missing absorb, store, and release energy, any reduction in total entropy generation would be stopped. Dispersion of NEPCMs, and MWCNTs, with their maximum volume fraction ($\varphi_{\mathbf{SNP}} = 0.025$, and $\varphi_{\mathbf{NEPCM}} = 0.025$), in the form of a hybrid nanofluid, inside the water host fluid maximizes the heat transfer rate, about 13 % more than the host fluid; simultaneously, the total entropy generation increases to under 5 % more than the water.

IV) Average Bejan number (Be_{AVG}) is a decreasing function than increasing Rayleigh number (Ra). The heat transfer entropy generation (S_θ) drives total entropy generation (S_T) in $Ra = 10^3$ and $Ra = 10^4$, where average Bejan number (Be_{AVG}) is more than 0.5. It is less than 0.5 ($Be_{AVG} < 0.5$) when $Ra = 10^5$, and consequently, the friction entropy generation (S_ψ) governs the total entropy generation (S_T). A constant value for average Bejan number (Be_{AVG}) was demonstrated by changing the value of

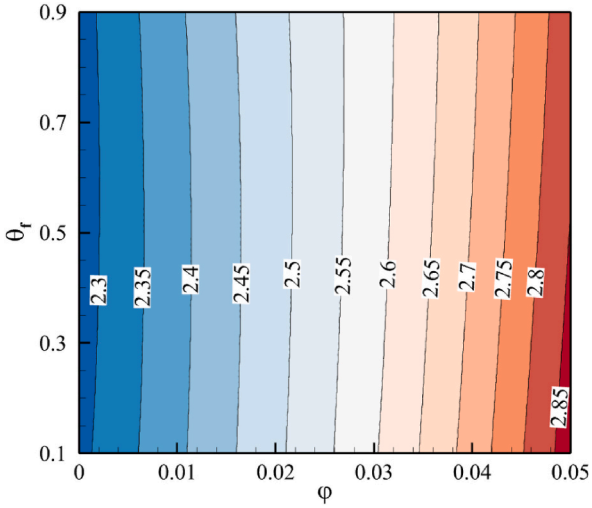

Fig. 15. The contours of hybrid nanoparticles volume fraction against the fusion temperature when Ra = 10000.

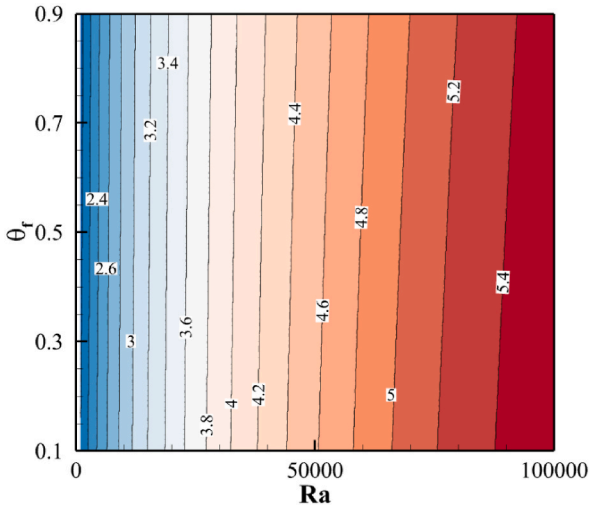

Fig. 16. The contours of fusion temperature against Rayleigh number when φ = 0.05.

nanoparticles volume fraction. It is because of equal enhancement of the heat transfer entropy generation (S_θ) and the total entropy generation (S_T).

V) The neural network successfully mapped the relationship between the control parameters and heat transfer rate. Using the trained neural network, the impact of fusion temperature, hybrid nanoparticle concentration, and Rayleigh number on the heat transfer rate was investigated. An increase in nanoparticles concentration and fusion temperature would notably increase the heat transfer rate.

CRediT authorship contribution statement

Mohamed Bouzidi: Writing – review & editing, Writing – original draft, Project administration, Methodology, Investigation, Formal analysis, Conceptualization. **Fathi Alimi:** Writing – original draft, Visualization, Methodology, Investigation, Formal analysis, Conceptualization. **Aeshah Alasmari:** Writing – original draft, Visualization, Resources, Funding acquisition, Formal analysis, Data curation, Conceptualization. **Mohammad S. Islam:** Writing – review & editing, Writing – original draft, Investigation, Formal analysis, Data curation, Conceptualization. **Pouyan Talebizadehsardari:** Writing – review & editing, Writing – original draft, Validation, Methodology, Formal analysis, Conceptualization. **Jana Shafi:** Writing – original draft, Visualization, Methodology, Investigation, Formal analysis, Data curation, Conceptualization. **Mehdi Ghalambaz:** Writing – review & editing, Supervision, Methodology, Conceptualization.

Declaration of competing interest

The authors clarify that there is no conflict of interest for report.

Data availability

Data will be made available on request.

Acknowledgments

The authors are thankful to the Deanship of Graduate Studies and Scientific Research at University of Bisha for supporting this work through the Fast-Track Research Support Program.

References

[1] J. Buongiorno, Convective Transport in Nanofluids, 2006.
[2] S. Hadi Hussain, A. Kadhim Hussein, Natural convection heat transfer enhancement in a differentially heated parallelogrammic enclosure filled with copper-water nanofluid, J. Heat Tran. 136 (8) (2014) 082502.
[3] M. Bouhalleb, H. Abbassi, Natural convection of nanofluids in enclosures with low aspect ratios, Int. J. Hydrogen Energy 39 (27) (2014) 15275–15286.
[4] R. Mohebbi, M. Izadi, N.A. Che Sidik, G. Najafi, Natural convection heat transfer of nanofluid inside a cavity containing rough elements using lattice Boltzmann method, Int. J. Numer. Methods Heat Fluid Flow 29 (10) (2019) 3659–3684.
[5] L. Snoussi, N. Ouerfelli, X. Chesneau, A.J. Chamkha, F.B.M. Belgacem, A. Guizani, Natural convection heat transfer in a nanofluid filled U-shaped enclosures: numerical investigations, Heat Tran. Eng. 39 (16) (2018) 1450–1460.
[6] S.A. Rozati, F. Montazerifar, O. Ali Akbari, S. Hoseinzadeh, V. Nikkhah, A. Marzban, H. Abdolvand, M. Goodarzi, Natural convection heat transfer of water/Ag nanofluid inside an elliptical enclosure with different attack angles, Math. Methods Appl. Sci. (2020). https://doi.org/10.1002/mma.7036.
[7] M.S. Khan, S. Ahmad, Z. Shah, N. Vrinceanu, M.H. Alshehri, Natural convection heat transfer of a hybrid nanofluid in a permeable quadrantal enclosure with heat generation, Case Stud. Therm. Eng. 56 (2024) 104207.
[8] A.V. Roşca, N.C. Roşca, I. Pop, M.A. Sheremet, Natural convection and entropy generation in a trapezoidal region with hybrid nanoliquid under magnetic field, Int. J. Numer. Methods Heat Fluid Flow 34 (2) (2024) 429–450.
[9] Q. Ali, M. Waqas, A. Mir, B.M. Alshammari, M. Amir, K.A. Khan, S.U. Khan, L. Kolsi, Prabhakar fractional model for natural convection flow for kerosene oil based hybrid nanofluid containing ferric oxide and zinc oxide nanoparticles, Case Stud. Therm. Eng. (2024) 104648.
[10] Y. Ouyang, M.F.M. Basir, K. Naganthran, I. Pop, Effects of discharge concentration and convective boundary conditions on unsteady hybrid nanofluid flow in a porous medium, Case Stud. Therm. Eng. 58 (2024) 104374.
[11] N.C. Roy, S. Monira, Magnetohydrodynamic natural convection of a reacting hybrid nanofluid in a porous wavy-walled cavity, ZAMM-Journal of Applied Mathematics and Mechanics/Zeitschrift für Angewandte Mathematik und Mechanik 104 (1) (2024) e202200476.
[12] Z. Han, B. Yang, S.H. Kim, M.R. Zachariah, Application of hybrid sphere/carbon nanotube particles in nanofluids, Nanotechnology 18 (10) (2007) 105701.
[13] P.S. Reddy, P. Sreedevi, A.J. Chamkha, MHD convective flow of SWCNTS-water and MWCNTS-water nanofluid over a vertical cone with thermal radiation and chemical reaction, J. Porous Media 26 (7) (2023) 47–68.
[14] P.S. Reddy, P. Sreedevi, Flow and heat transfer analysis of carbon nanotubes based nanofluid flow inside a cavity with modified Fourier heat flux, Phys. Scripta 96 (5) (2021) 055215.
[15] P.S. Reddy, P. Sreedevi, V.N. Reddy, Entropy generation and heat transfer analysis of magnetic nanofluid flow inside a square cavity filled with carbon nanotubes, Chemical Thermodynamics and Thermal Analysis 6 (2022) 100045.
[16] T. Tayebi, A.J. Chamkha, Magnetohydrodynamic natural convection heat transfer of hybrid nanofluid in a square enclosure in the presence of a wavy circular conductive cylinder, J. Therm. Sci. Eng. Appl. 12 (3) (2020) 031009.
[17] I. Chabani, F. Mebarek-Oudina, H. Vaidya, A. Ismail, Numerical analysis of magnetic hybrid Nano-fluid natural convective flow in an adjusted porous trapezoidal enclosure, J. Magn. Magn Mater. 564 (2022) 170142.
[18] M.M. Rahman, Z. Saghir, I. Pop, Free convective heat transfer efficiency in Al2O3–Cu/water hybrid nanofluid inside a rectotrapezoidal enclosure, Int. J. Numer. Methods Heat Fluid Flow 32 (1) (2022) 196–218.
[19] H.T. Kadhim, A. Al-Manea, A.N. Al-Shamani, T. Yusaf, Numerical analysis of hybrid nanofluid natural convection in a wavy walled porous enclosure: local thermal non-equilibrium model, International Journal of Thermofluids 15 (2022) 100190.
[20] A. Alsabery, H. Kadhim, M. Ismael, I. Hashim, A. Chamkha, Impacts of amplitude and heat source on natural convection of hybrid nanofluids into a wavy enclosure via heatline approach, Waves Random Complex Media 33 (4) (2023) 1060–1084.
[21] R. Hidki, L. El Moutaouakil, M. Boukendil, Z. Charqui, Z. Zrikem, A. Abdelbaki, Impact of Cu, Al2O3-water hybrid nanofluid on natural convection inside a square cavity with two heat-generating bodies, Mater. Today: Proc. 72 (2023) 3749–3756.
[22] P. Sreedevi, P.S. Reddy, Entropy generation and heat transfer analysis of alumina and carbon nanotubes based hybrid nanofluid inside a cavity, Phys. Scripta 96 (8) (2021) 085210.
[23] T. Scott, D. Ewim, A. Eloka-Eboka, Experimental study on the influence of volume concentration on natural convection heat transfer with Al2O3-MWCNT/water hybrid nanofluids, Mater. Today: Proc. (2023). https://doi.org/10.1016/j.matpr.2023.07.290.
[24] T.O. Scott, D.R. Ewim, A.C. Eloka-Eboka, Experimental investigation of natural convection Al2O3-MWCNT/water hybrid nanofluids inside a square cavity, Exp. Heat Tran. 37 (3) (2024) 294–312.
[25] P.S. Reddy, P. Sreedevi, M. Ghalambaz, Heat transfer investigation of nano–Encapsulated phase change materials (NEPCMs) in a thermal energy storage device, Appl. Therm. Eng. (2024) 123495.
[26] P. Reddy, P. Sreedevi, Enhanced entropy generation and heat transfer characteristics of magnetic nano-encapsulated phase change materials in latent heat thermal energy storage systems, Appl. Math. Mech. 45 (6) (2024) 1051–1070.
[27] W. Li, S. Guo, L. Tan, L. Liu, W. Ao, Heat transfer enhancement of nano-encapsulated phase change material (NEPCM) using metal foam for thermal energy storage, Int. J. Heat Mass Tran. 166 (2021) 120737.
[28] F. Mebarek-Oudina, I. Chabani, H. Vaidya, A.A.I. Ismail, Hybrid-nanofluid magneto-convective flow and porous media contribution to entropy generation, Int. J. Numer. Methods Heat Fluid Flow 34 (2) (2024) 809–836.
[29] M.A. Alomari, F.H. Ali, Q.H. Al-Salami, H.K. Hamzah, Q.R. Al-amir, F.Q. Alyousuf, M.A. Ismael, Numerical analysis of MHD free convection in curvilinear porous enclosure with two active cylinders filled with NE-phase change material, J. Energy Storage 95 (2024) 112602.
[30] H. Saleh, R. Muhandaz, A. Irma, I. Fitri, D. Fitraini, A. Sari, H. Nufus, Free convection from a localized heated cylinder with nano encapsulated phase change material and water in a square enclosure, J. Energy Storage 56 (2022) 106028.
[31] A.F. Turki, O.S. Mahdy, N.H. Abu-Hamdeh, D.J. Jasim, A.H. Milyani, H. Kazemi-Varnamkhasti, A.a. Alizadeh, N. Nasajpour-Esfahani, D. Toghraie, Investigating the thermal performance of nano-encapsulated phase change materials-water nanofluid in the presence of a heat source as applied in electronic devices, J. Taiwan Inst. Chem. Eng. 150 (2023) 105030.
[32] M. Ghalambaz, M.A. Sheremet, I. Pop, Free convection in a parallelogrammic porous cavity filled with a nanofluid using Tiwari and Das' nanofluid model, PLoS One 10 (5) (2015) e0126486.

[33] S. Barlak, O.N. Sara, A. Karaipekli, S. Yapıcı, Thermal conductivity and viscosity of nanofluids having nanoencapsulated phase change material, Nanoscale Microscale Thermophys. Eng. 20 (2) (2016) 85–96.
[34] G. Venkatesan, G.-P. Jin, M.-C. Chyu, J.-X. Zheng, T.-Y. Chu, Measurement of thermophysical properties of polyurethane foam insulation during transient heating, Int. J. Therm. Sci. 40 (2) (2001) 133–144.
[35] D. Pau, C. Fleischmann, M. Spearpoint, K. Li, Thermophysical properties of polyurethane foams and their melts, Fire Mater. 38 (4) (2014) 433–450.
[36] M. Ghalambaz, M. Sabour, I. Pop, D. Wen, Free convection heat transfer of MgO-MWCNTs/EG hybrid nanofluid in a porous complex shaped cavity with MHD and thermal radiation effects, Int. J. Numer. Methods Heat Fluid Flow 29 (11) (2019) 4349–4376.
[37] S. Kuravi, K.M. Kota, J. Du, L.C. Chow, Numerical Investigation of Flow and Heat Transfer Performance of Nano-Encapsulated Phase Change Material Slurry in Microchannels, 2009.
[38] K. Kahveci, Buoyancy Driven Heat Transfer of Nanofluids in a Tilted Enclosure, 2010.
[39] J.R. Babu, K.K. Kumar, S.S. Rao, State-of-art review on hybrid nanofluids, Renew. Sustain. Energy Rev. 77 (2017) 551–565.
[40] K. Khanafer, K. Vafai, A critical synthesis of thermophysical characteristics of nanofluids, in: Nanotechnology and Energy, Jenny Stanford Publishing, 2017, pp. 279–332.
[41] S.M. Seyyedi, A. Dogonchi, D. Ganji, M. Hashemi-Tilehnoee, Entropy generation in a nanofluid-filled semi-annulus cavity by considering the shape of nanoparticles, J. Therm. Anal. Calorim. 138 (2) (2019) 1607–1621.
[42] A.A. Sakhir Abed, Numerical simulation of laminar incompressible driven cavity flow in a l-shape domain, Int. J. Mech. Eng. Technol. 10 (1) (2019) 119–132.
[43] S. Mehryan, M. Ghalambaz, L.S. Gargari, A. Hajjar, M. Sheremet, Natural convection flow of a suspension containing nano-encapsulated phase change particles in an eccentric annulus, J. Energy Storage 28 (2020) 101236.
[44] M.h. Souli, D.J. Benson, Arbitrary Lagrangian Eulerian and Fluid-Structure Interaction: Numerical Simulation, John Wiley & Sons, 2013.
[45] R. Codina, G. Houzeaux, H. Coppola-Owen, J. Baiges, The fixed-mesh ALE approach for the numerical approximation of flows in moving domains, J. Comput. Phys. 228 (5) (2009) 1591–1611.
[46] J. Raza, F. Mebarek-Oudina, H. Ali, I. Sarris, Slip effects on casson nanofluid over a stretching sheet with activation energy: RSM analysis, Frontiers in Heat and Mass Transfer 22 (4) (2024) 1017–1041.
[47] M. Ghalambaz, A.J. Chamkha, D. Wen, Natural convective flow and heat transfer of nano-encapsulated phase change materials (NEPCMs) in a cavity, Int. J. Heat Mass Tran. 138 (2019) 738–749.
[48] J. Moolayil, J. Moolayil, S. John, Learn Keras for Deep Neural Networks, Springer, 2019.
[49] A. Gulli, S. Pal, Deep Learning with Keras, Packt Publishing Ltd, 2017.
[50] N.K. Manaswi, N.K. Manaswi, Understanding and Working with Keras, Deep Learning with Applications Using Python: Chatbots and Face, Object, and Speech Recognition with TensorFlow and Keras, 2018, pp. 31–43.
[51] N. Ketkar, N. Ketkar, Introduction to Keras, Deep Learning with python: a Hands-On Introduction, 2017, pp. 97–111.
[52] Z. Zhang, Improved adam optimizer for deep neural networks, in: 2018 IEEE/ACM 26th International Symposium on Quality of Service (IWQoS), Ieee, 2018, pp. 1–2.